


 Cite this: *RSC Adv.*, 2021, **11**, 4256

# A comparative electrochemical study of non-enzymatic glucose, ascorbic acid, and albumin detection by using a ternary mesoporous metal oxide ( $ZrO_2$ , $SiO_2$ and $In_2O_3$ ) modified graphene composite based biosensor

 Kamrun Nahar Fatema<sup>a</sup> and Won-Chun Oh<sup>ib</sup>  <sup>\*ab</sup>

In this study, we present an electrochemical investigation of a ternary mesoporous metal oxide ( $ZrO_2$ ,  $SiO_2$  and  $In_2O_3$ ) modified graphene composite for non-enzymatic glucose, ascorbic acid, and albumin detection in urine at physiological pH. Synergetic property of  $ZrO_2$ -Ag-G- $SiO_2$  and  $In_2O_3$ -G- $SiO_2$  were investigated via cyclic voltammetry (CV) using FTO glass and copper-foil electrodes with no prerequisite of solid antacid expansion. The mesoporous  $ZrO_2$ -Ag-G- $SiO_2$  and  $In_2O_3$ -G- $SiO_2$  composites were synthesized and characterized using XRD, SEM, TEM, Raman spectroscopy, XPS, DRS, BET, and photocurrent measurements. Upon increasing the glucose concentration from 0 to 3 mM, CV results indicated two anodic peaks at +0.18 V and +0.42 V *versus* Ag/AgCl, corresponding to  $Zr^{3+}$  and  $Zr^{4+}$ , respectively, considering the presence of glucose in urine. Moreover, the effects of high surface area  $In_2O_3$ -G- $SiO_2$  were observed upon the examination of  $ZrO_2$ -Ag-G- $SiO_2$ .  $In_2O_3$ -G- $SiO_2$  demonstrated a decent electrochemical pattern in glucose, ascorbic acid, and albumin sensing. Nevertheless, insignificant synergistic effects were observed in  $In_2O_3$ -G,  $ZrO_2$ -G, and  $ZrO_2$ -G- $SiO_2$ .  $In_2O_3$ -G- $SiO_2$  performed well under a wide range of electrolytes and urine, and showed no activity toward uric acid, suggesting potential for biodetection in urine.

Received 21st November 2020

Accepted 15th December 2020

DOI: 10.1039/d0ra09886h

[rsc.li/rsc-advances](http://rsc.li/rsc-advances)

## 1. Introduction

Diabetes mellitus has become a universally critical health challenge that has caused other non-transferable sicknesses and complications such as cardiovascular illness, stroke, and chronic kidney failure.<sup>1</sup> Non-obtrusive glucose and micro-albumin estimation has largely improved the treatment viability and preventive measures. For simple glucose level determination, an assessment of glucose in urine can be a decent marker,<sup>2-5</sup> as glucose is released in the body because of kidney failure, endocrine issues, and hyperglycemia. Recent improvements in non-enzymatic glucose detection has overcome the restrictions of traditional chemical-based glucose sensors, influenced by humidity, pH, protein denaturation, poor reproducibility, and significant manufacturing cost.<sup>6</sup> According to Pletcher,<sup>7</sup> the working of a non-enzymatic glucose sensor involves the chemisorption of hydroxyl ions onto a metal substrate, permitting a bond formation between the d-electrons

of the metal and glucose. Accordingly, a difference in the oxidation state of glucose molecules adsorbed onto the metal surface leads to a difference in the metal–glucose complex, lowering the quality of the glucose–metal bond and in turn lowering the desorption rate of glucose molecules.<sup>6-8</sup> The impersonating cycle of metals and metal oxides, such as Au, Cu, Pt, Ni *etc.*,<sup>9-18</sup> have been accounted by the direct electrochemical oxidation of glucose and electron move. Among these metals,  $ZrO_2$  based substrates have been considered as the best because of their ease of production, high strength, and excellent synergistic properties.  $ZrO_2$  is one of the metal oxides with oxidizable and reducible sites.  $ZrO_2$  is an n-type semiconductor with a bandgap of 5.12 eV.<sup>19</sup> Subsequently, the modification of  $ZrO_2$  with other supporting materials, such as graphene oxide and/or another p-type semiconductor, is a promising way to achieve the above-mentioned objectives, particularly enhancing its synergistic properties.

Graphene-based metal oxide materials have remarkable applications in various fields. Furthermore, the oxygen-containing-functional groups of graphene oxide act as a stabilizer for the metal-nanoparticles and prevent their aggregation. However, despite the high reaction kinetics and electron transfer, activity in highly alkaline conditions is insignificant for the vast majority of physiological samples. A powerful

<sup>a</sup>Department of Advanced Materials Science & Engineering, Hanseo University, Seosan-si, Chungnam, Korea, 356-706. E-mail: wc\_oh@hanseo.ac.kr; Fax: +82-41-688-3352; Tel: +82-41-660-1337

<sup>b</sup>College of Materials Science and Engineering, Anhui University of Science & Technology, Huainan 232001, PR China



technique for enhancing the performance of graphene is to improve the electron-donating capacity, charge/discharge capacity, and resistance of graphene.<sup>20</sup>

Mesoporous silica, made of silica aerogel, has been used as a substrate material, adsorbent, and thermal insulator. In the field of catalysis, it can provide a high density of surface area to be used as an adsorbent.<sup>21</sup> The main reason for the progress of graphene-based metal oxide photocatalysts is that carbon material (graphene) can influence the rate at which photo-generated electrons relocate from the metal oxide to graphene and reduce the electron-hole recombination.<sup>22</sup> The combination of the stability of  $ZrO_2$  and high-surface area of mesoporous  $SiO_2$  with graphene can lead to enhanced reaction kinetics.

Ascorbic acid (AA, nutrient C) is an exceptionally huge bioactive compound and a water-soluble nutrient that cannot be synthesized by the human body, and should, therefore, be introduced through daily diet. Ascorbic acid is added to a few drug formulations to boost injury recovery<sup>23</sup> and to prevent or cure some diseases, such as scurvy,<sup>24</sup> normal cold,<sup>25</sup> and hyphema.<sup>26</sup> Moreover, AA is the most unstable nutrient in food, especially products of the soil, and its decomposition leads to a decline in the wholesome food quality.<sup>27</sup> Accordingly, a detection strategy that allows a fast, simple, and sensitive detection of AA would be significant in various fields, especially in medicine and the food industry.

In this work, we studied mesoporous  $ZrO_2$ -Ag-G- $SiO_2$  and  $In_2O_3$ -G- $SiO_2$  substrates without precedent for non-commercial urine and PBS. We carried out experiments to determine the direct correlation of the electrocatalytic characteristics of  $ZrO_2$ -Ag-G- $SiO_2$  and  $In_2O_3$ -G- $SiO_2$ . The analyses were performed using FTO glass and copper foil electrodes *via* cyclic voltammetry (CV) to obtain the reaction mechanism. Moreover, the effects of carbon framework, such as graphene (G), on  $ZrO_2$  and  $In_2O_3$  were assessed in both basic and neutral pH conditions. Also, the morphological, physical, and chemical properties of  $ZrO_2$ -Ag-G- $SiO_2$  and  $In_2O_3$ -G- $SiO_2$  were studied. In general,  $ZrO_2$ -Ag-G- $SiO_2$  and  $In_2O_3$ -G- $SiO_2$  exhibited an excellent performance in inert media without any electron donor, indicating further progress for basic glucose, albumin, and ascorbic acid determination in urine.

## 2. Experimental section

### 2.1. Materials

All chemical reagents of analytical grade were used without further purification. Graphite powder flakes (>99.99 wt%), zirconium(IV) propoxide ( $C_{12}H_{28}O_4Zr$ , 70 wt% in 1-propanol), and Pluronic F127 ( $EO_{106}PO_{70}EO_{106}$ ) were procured from Sigma-Aldrich;  $InCl_3$  indium(III) chloride, urea, SDBS - sodium dodecyl benzene sulphonate, and tetraethyl orthosilicate (TEOS, Acros Organics) were procured from Samchun Pure Chemical Co Ltd. Ethylene glycol ( $C_2H_6O_2$ , 99.5%) was purchased from Duksan Pure Chemicals Co. Ltd., Korea; hydrochloric acid (HCl) was purchased from Dae-Jung Chemical Co. Ltd., Korea. Deionized water ( $18.2\text{ M}\Omega\text{ cm}^{-1}$ ) was used in all the experiments.

**2.1.1. Synthesis of graphene oxide.** A modified Hummers' method was used to synthesize graphene oxide by the oxidation of graphite powder.<sup>28</sup> 15 g common graphite and sulfuric acid (450 mL,  $H_2SO_4$ ) were added to de-ionized water and stirred for an hour at 0 °C in an ice bath. After 1 h, the ice bath was removed and potassium permanganate (45 g,  $KMnO_4$ ) was slowly added to the mixture (graphite +  $H_2SO_4$ ) and stirred continuously at 35 °C until the color of the mixture changed to gray. The reaction vessel was fixed and maintained at 100 °C while stirring for 30 min. Hydrogen peroxide ( $H_2O_2$ ) was then added dropwise over 5 min. The mixture was washed with  $(CH_3)_2CO$  and hydrochloric acid (HCl, 10%) a few times, and then heated in an oven at 90 °C for 12 h until it turned into graphite oxide powder. The as-obtained graphite oxide powder was added to 200 mL de-ionized water, thoroughly stirred for 30 min, and then ultrasonicated for 2 h (using Ultrasonic Processor, VCX 750). Finally, the mixture was filtered and washed with warm water a few times, and then placed in the oven for 6 h to form graphene oxide powder.

**2.1.2. Synthesis of  $ZrO_2$ .** 6 g Pluronic F127 was poured into 30 mL of anhydrous ethanol to make mixture A. Then, 30 mL of zirconium(IV) propoxide mixture was blended with 30 mL mixture of ethanol and ethylene glycol, used as a stabilizer, to make mixture B with vigorous stirring. Mixtures A and B were combined and mixed under 40 °C, followed by the dropwise addition of 20 mL of de-ionized water. A suitable volume of hydrochloric acid was added to adjust the pH to 2.4, and the mixture was stirred at 40 °C for 1 h. The subsequent mixture was kept at 40–80 °C in a closed compartment for 24 h until it formed a gel. The precipitate was filtered through a Whatman filter paper ( $\Phi = 110$  mm), and further dried at 100 °C in an electric oven. The as-synthesized materials were then calcined at 400 °C for 4 h to remove the template. To evaluate the thermal stability, the samples without the template were calcined in air at a temperature of 600 °C for 4 h.

**2.1.3. Combining GO with  $ZrO_2$ .** 0.333 g of GO was dispersed in 200 mL of de-ionized water and exposed to sonication (amp = 70%, power = 840 Watt) for 30 min to make mixture C. Meanwhile,  $ZrO_2$  was dissolved to make mixture D through vigorous mixing; then, this mixture was mixed with C. 31.5 mL of 1 M sodium hydroxide (NaOH) was added dropwise into the sonicated precursor to create an ideal pH. The resultant mixture was stirred for 1 h under 100 °C until the mixture color changed to black, and this modification led to the successful combination of GO with  $ZrO_2$  to form mixture E.

**2.1.4. Combining  $SiO_2$  with G- $ZrO_2$ .** 1.0 g of triblock copolymer Pluronic F-127 was added to 15 mL of deionized water and 60 mL (2 M) HCl and stirred at 40 °C until the copolymer was completely dissolved. 3.20 g of tetraethyl orthosilicate (TEOS) was added and the solution was stirred for 12 h at 40 °C. The mixture was transferred into a 100 mL capacity stainless steel-lined autoclave and kept at 100 °C in the container for 20 h. The subsequent white precipitate was separated through a Whatman filter paper ( $\Phi = 110$  mm), washed with de-ionized water and ethanol a few times, and then dried under vacuum at 65 °C overnight. Finally, the powder was



calcined in air at 550 °C for 3 h to eliminate the copolymer. Mixture E was added dropwise into a 100 mL round-bottom flask containing 0.3 g of silica powder and stirred at 100 °C for 24 h. After 24 h, ultrasonication (amp = 70%, power = 840 Watt) was carried out for 1 h, after which the mixture was filtered, washed with 1 mL of methanol, and dried under vacuum at 65 °C overnight. The furnace temperature was increased to 700 °C at a rate of 10 °C min<sup>-1</sup> and held at 700 °C for 4 h. Finally, the furnace was gradually cooled to room temperature (RT; +25 °C), and the color of the final product was dark brown or black.

**2.1.5 Mesoporous silica synthesis with In<sub>2</sub>O<sub>3</sub>–GO.** 1.0 g of triblock copolymer Pluronic P-127 surfactant (Aldrich) was added to a reaction vessel containing 15 g of deionized water and 60 g of 2 M HCl at 40 °C and then stirred until the copolymer was completely dissolved. 3.20 g of tetraethyl orthosilicate (TEOS, Acros Organics) was added and stirred for 12 h at 40 °C. The mixture was heated to 100 °C in an oven for 20 h. The subsequent white precipitate was filtered, washed with water and ethanol, and dried at 65 °C in a short period. Finally, the copolymer was eliminated by calcination in air at 550 °C for 3 h. The combined mesoporous In<sub>2</sub>O<sub>3</sub> nanoparticles were dispersed in 7 mL of deionized water, followed by the addition of GO water suspension comparative with the amount of incorporated mesoporous In<sub>2</sub>O<sub>3</sub> nanoparticles in the mixture. GO was obtained from graphite flakes by using the Hummers' method. The combined mesoporous In<sub>2</sub>O<sub>3</sub> nanoparticles were scattered in 7 mL of deionized water, followed by the addition of GO water suspension comparative with the amount of incorporated mesoporous In<sub>2</sub>O<sub>3</sub> nanoparticles in the mixture. The mixture was ultra-sonicated for 20 min, and the In<sub>2</sub>O<sub>3</sub>–GO mixture was added dropwise to a 100 mL round-bottom flask containing silica powder in two different proportion, 10% and 20%. After mixing for 48 h, the powder was filtered, washed with 1 mL of methanol, and dried at 70 °C in a short period. The furnace temperature was increased to 700 °C at a rate of 10 °C min<sup>-1</sup> and held at 700 °C for 4 h. Finally, the furnace was gradually cooled to room temperature. A light yellow colored product was obtained.

## 2.2. Characterization

The phases of the samples were examined using X-ray diffraction measurements (SHIMADZU XRD-6000) equipped with a Cu K $\alpha$  X-ray source (1.5406 Å). The Debye–Scherrer equation (eqn (1)) was used to determine the particle size of ZrO<sub>2</sub> and SiO<sub>2</sub>, based on the data acquired *via* XRD analysis.<sup>17</sup>

$$L = K\lambda/(FWHM)\cos \theta; [d = 0.9\lambda/\beta \cos \theta] \quad (1)$$

where  $L$  is the particle size,  $\lambda$  is the wavelength of X-ray radiation (1.5406 Å),  $\beta$  is the full width at half maximum (FWHM) of the peak (in radians), and  $2\theta$  is the Bragg angle. The shape and structure of the nanomaterial surface were analyzed using a high-resolution SEM (TESCAN, MAIA3). The chemical composition was analyzed using energy dispersive X-ray (EDX) analysis in combination with SEM. Transmission electron microscopy (TEM, Hitachi HT7700, operated at 100 kV) was used to analyze the morphologies of the samples. High-resolution transmission electron microscopy (HRTEM) images

of the samples were obtained using a Hitachi H9500 operated at 300 kV. Raman spectroscopy was performed using a confocal Raman imaging system with a 633 nm excitation laser (Renishaw inVia Reflex). The surface composition was analyzed *via* X-ray photoelectron spectroscopy (SHIMADZU, KRATOS AXIS SUPRA) with a monochromatized Al K $\alpha$  X-ray source (10 kV, 1500 W, pass energy = 40 eV). UV-vis diffuse reflectance spectroscopy (DRS) was performed using an ultraviolet-visible (UV-vis) spectrophotometer (SHIMADZU UV-2600) ranging from 200 to 800 nm. The bandgap energies of the photocatalysts were calculated through the application of a modified Kubelka–Munk function obtained from the UV-vis DRS data. Nitrogen adsorption/desorption isotherms were analyzed by Micro Active for ASAP 2460, the specific surface area was calculated by the Brunauer–Emmett–Teller (BET) method, and pore-size distribution was evaluated according to the Barrett–Joyner–Halenda (BJH) method. Photoluminescence spectra (PL) were obtained by a fluorescence spectrophotometer (Hitachi F-7000) with an emission wavelength region of 280–500 nm at RT.

## 2.3 Electrode preparation and measurements

In<sub>2</sub>O<sub>3</sub>–G–SiO<sub>2</sub> and ZrO<sub>2</sub>–Ag–G–SiO<sub>2</sub> thin films were prepared using a conventional atomic layer deposition technique.<sup>29</sup> In<sub>2</sub>O<sub>3</sub>, IG, mesoporous IGS10, and IGS20 individually were ground with ethyl cellulose and PVDF in an agate mortar to form a gas detecting paste. The paste was coated on a substrate by applying a physical coating method and it is important that the paste evenly applied on the surface. The as-prepared coated-substrate put into an electric oven and dried at 100 °C for 3 h. The paste was coated manually *via* a physical coating method. The thickness of the coating was 0.1, 0.3, and 0.5 mm, and all the samples had uniform thickness and measurements. An electrochemical cell was used in voltammetry with three electrodes: a working electrode (WE), reference electrode (RE), counter electrode (CE). A cyclic low potential excitation signal was applied between the working electrode and the reference electrode and the current flowing between the working and reference electrodes was estimated. The current peaks were obtained at a specific voltage region, due to the specific redox potentials running on the working terminal. The reference electrode was used for the analysis of the Cyclic Voltammetry (CV). The signal conditioning stage applied time-dependent potential between the working and reference electrodes, and converted the current flowing between the working and reference electrodes into a voltage signal.

## 3. Result and discussion

### 3.1. Material characterizations

Fig. 1 shows the XRD patterns of ZrO<sub>2</sub>–GO, GO–SiO<sub>2</sub>, and ZrO<sub>2</sub>–GO–SiO<sub>2</sub> nanocomposites, and the pattern essentially shows the structural phases of all materials studied. The main (green colored) peak presents the XRD pattern of ZrO<sub>2</sub>–GO nanocomposites, which correspond to the two crystalline phases, monoclinic ( $a = 5.1477$  Å,  $b = 5.2096$  Å,  $c = 5.3164$  Å) and tetragonal ( $a = 3.5781$  Å,  $c = 5.1623$  Å), and the reference numbers are JCPDS no. 78-0047, and no. 88-1007.<sup>18</sup> The peaks



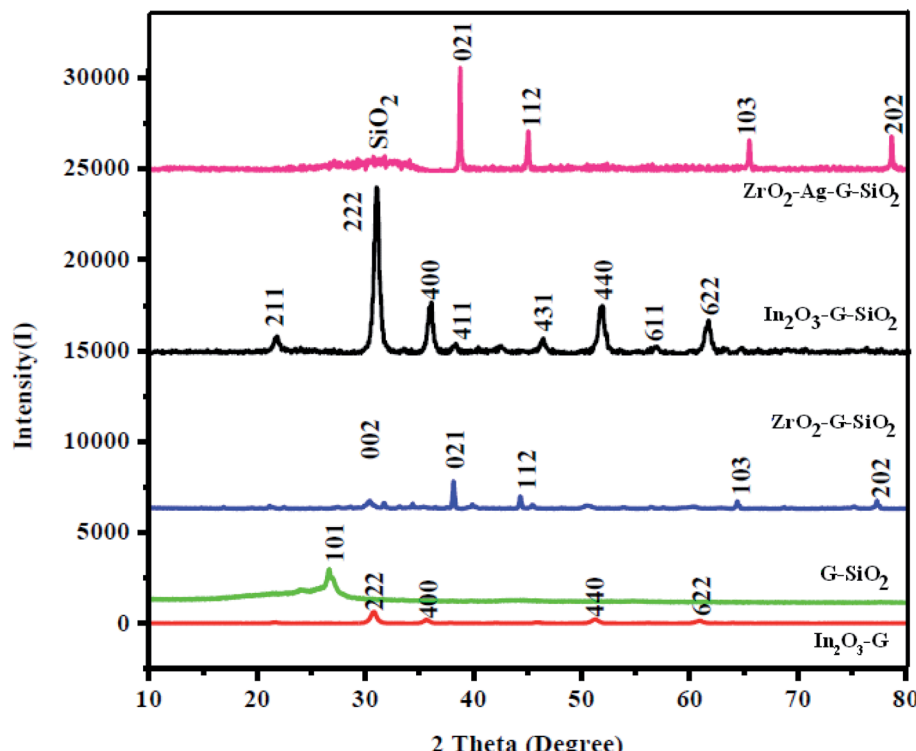


Fig. 1 XRD patterns of (a)  $\text{In}_2\text{O}_3$ -GO, (b) G-SiO<sub>2</sub>, (c) Zr-G-SiO<sub>2</sub> (d)  $\text{In}_2\text{O}_3$ -GO-SiO<sub>2</sub>, (e) Zr-Ag-G-SiO<sub>2</sub>.

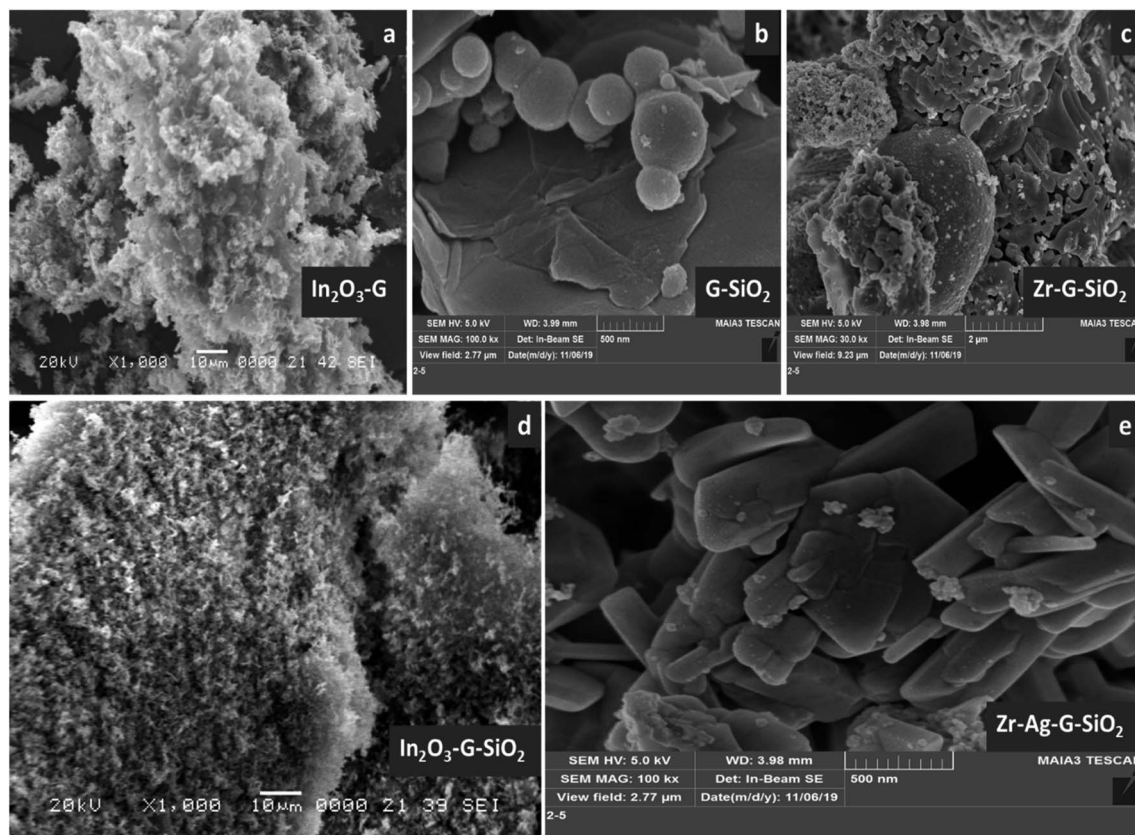


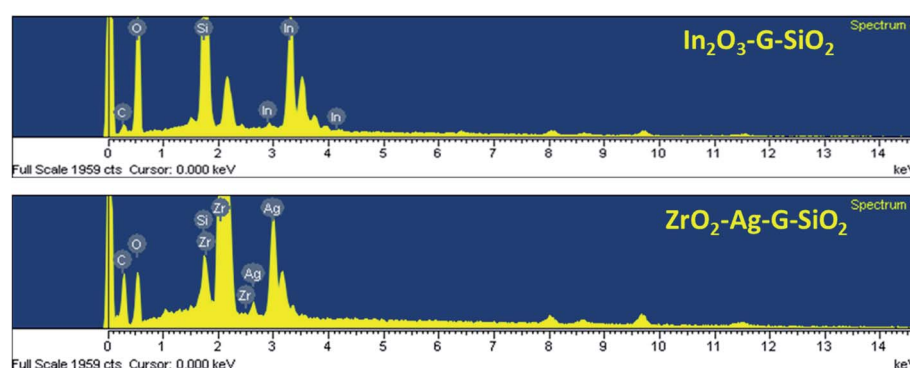
Fig. 2 SEM images of (a)  $\text{In}_2\text{O}_3$ -GO, (b) G-SiO<sub>2</sub>, (c) Zr-G-SiO<sub>2</sub> (d)  $\text{In}_2\text{O}_3$ -GO-SiO<sub>2</sub>, (e) Zr-Ag-G-SiO<sub>2</sub>.

were located at 30.63, 35.49, 50.84, 60.46° 2 $\theta$  assigned to the (002), (101), (102), and (103) planes, respectively, and this result suggested a base-centered monoclinic structured ZrO<sub>2</sub>. And the other diffraction peaks corresponded to the tetragonal structured ZrO<sub>2</sub>. The diffraction peak ratio between tetragonal and monoclinic was 7 : 3. The subsequent pattern (orange colored) presents the XRD data of GO–SiO<sub>2</sub> nanocomposites; this pattern demonstrated a sharp and wide peak, which was situated at a 2 $\theta$  of 26.62°. The last pattern (wine colored) presents the XRD of the ternary ZrO<sub>2</sub>–GO–SiO<sub>2</sub> composite. All the characteristic peaks were present, which were allocated to ZrO<sub>2</sub>, SiO<sub>2</sub>, and graphene. Also, the XRD pattern of the ternary composite had a new peak, implying that ZrO<sub>2</sub> and mesoporous SiO<sub>2</sub> undergo slight structural changes to give another XRD peak. The XRD pattern of the binary composite did not show the diffraction peaks of the graphitic material because of the exceptionally low amounts. Furthermore, the XRD results affirmed that mesoporous SiO<sub>2</sub> is effectively attached to GO and ZrO<sub>2</sub> nanocomposite; additionally, the arrangement strategy is demonstrated to be the best possible combination cycle of the material. We used the Debye–Scherrer formula to assess the crystallite size of ZrO<sub>2</sub> and SiO<sub>2</sub> particles and discovered them to be 72 and 15 nm, respectively.

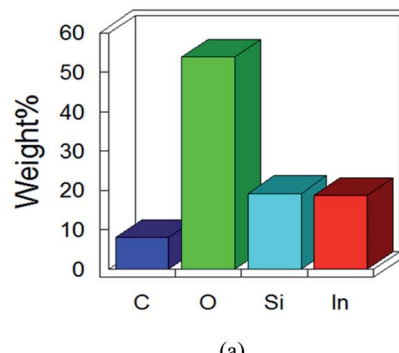
Fig. 2 presents the overall morphology of the as-obtained binary and ternary composites investigated through SEM examination. As shown in Fig. 2(a, b) and (c–e), from the SEM

investigation of the consequent GO–SiO<sub>2</sub> and ZrO<sub>2</sub>–GO double composite, the unpredictable 3D cubic ZrO<sub>2</sub> and spherical SiO<sub>2</sub> were consistently dispersed onto the graphene surface. The normal particle size of ZrO<sub>2</sub> was 55.04 nm, and the diameter of SiO<sub>2</sub> was 280.21 nm.<sup>19</sup> Fig. 2(e) shows that the growth of metal oxide and silica oxide completely covered the whole surface of graphene. The primary oxide compound shape was not changed; however, the size of silica oxide was diminished after adsorption onto the graphene surface. The principle function of graphene was to provide sufficient area of nanocomposite that can be developed and spread (attached) on the surface during the combination cycle. Moreover, graphene forms a covalent bond with the precursors through oxygen-containing functional groups. The results of SEM demonstrated the differences between the paired and ternary composite.

Fig. 3 presents the consequent laboratory-scale examination of a ternary (ZrO<sub>2</sub>–GO–SiO<sub>2</sub>) composite, which uncovers the fundamental components, in particular C, O, Zr, and Si. The component of C was obtained from graphene. Zr and Si are the fundamental components in ZrO<sub>2</sub> and SiO<sub>2</sub>. The nuclear and weight amounts of oxygen were high due to the ternary composite comprising of an oxide segment and graphene oxide. Also, a few peaks were seen in the EDX spectra because of a part of the precursor material and contamination from the machine. The shape and morphology of the binary and ternary composites were observed and examined using TEM and HRTEM, and

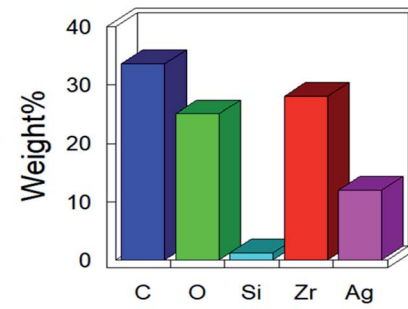


Quantitative results



(a)

Quantitative results



(b)

Fig. 3 EDS of (a) In<sub>2</sub>O<sub>3</sub>–GO–SiO<sub>2</sub> and (b) Zr–Ag–G–SiO<sub>2</sub> samples.

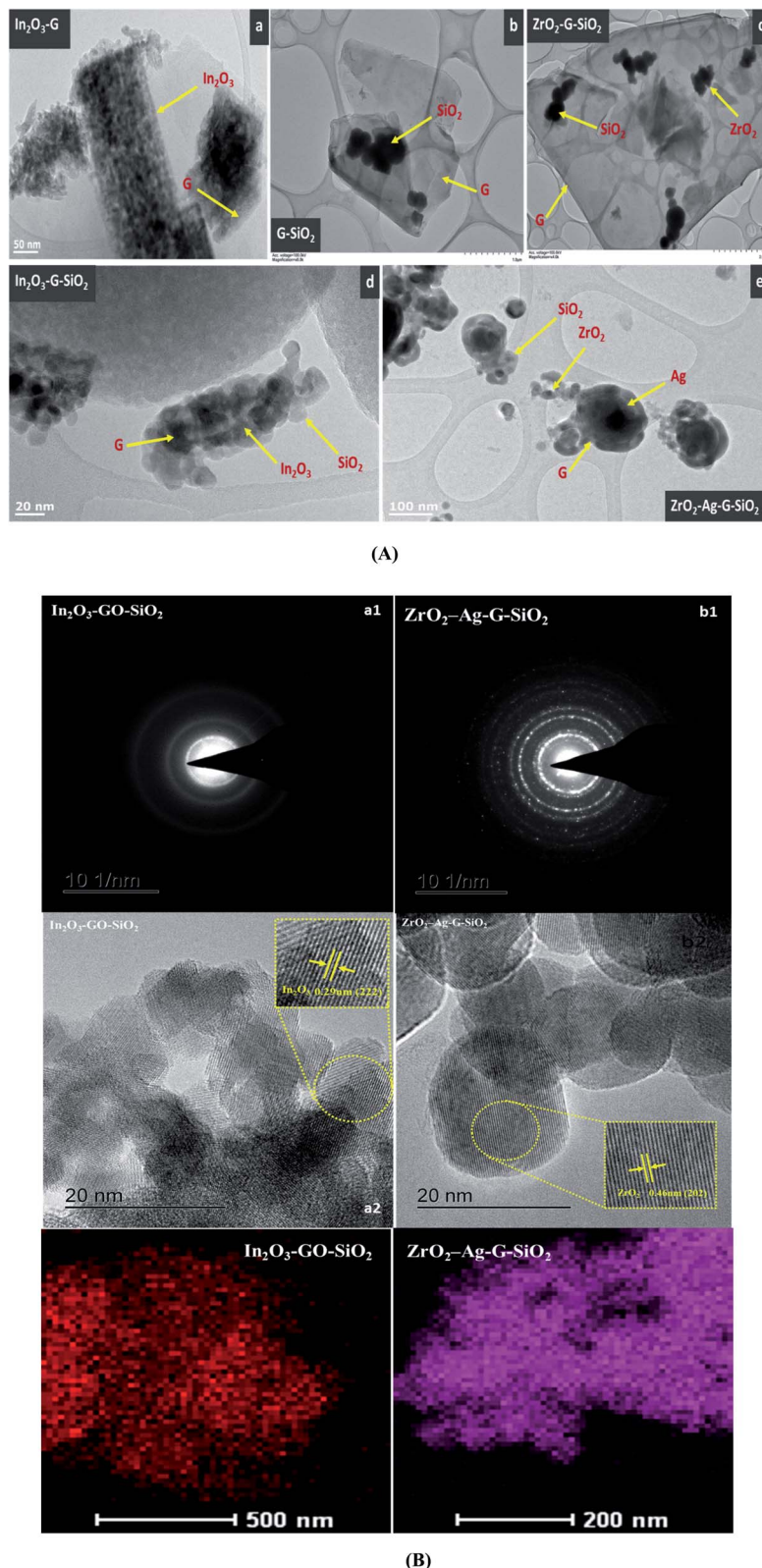


Fig. 4 TEM images (A) of (a)  $\text{In}_2\text{O}_3$ -GO, (b)  $\text{G-SiO}_2$ , (c)  $\text{Zr-G-SiO}_2$  (d)  $\text{In}_2\text{O}_3$ -GO- $\text{SiO}_2$ , (e)  $\text{Zr-Ag-G-SiO}_2$ . HRTEM images (B) and SAED pattern (B) of  $\text{In}_2\text{O}_3$ -GO- $\text{SiO}_2$  (a1 and a2) and  $\text{Zr-Ag-G-SiO}_2$  (b1 and b2) nanocomposites, respectively.

Fig. 4(A) shows images with different magnifications. The metal oxide ( $\text{ZrO}_2$ ) nanocomposite appeared as a dark spot in Fig. 4(a) and (b). Silica oxide ( $\text{SiO}_2$ ) was round, and was dull colored, as

shown in Fig. 4(c) and (d). The silica oxide nanocomposites were agglomerated on the surface of graphene. The silica and modified metal oxide nanocomposites were surrounded by

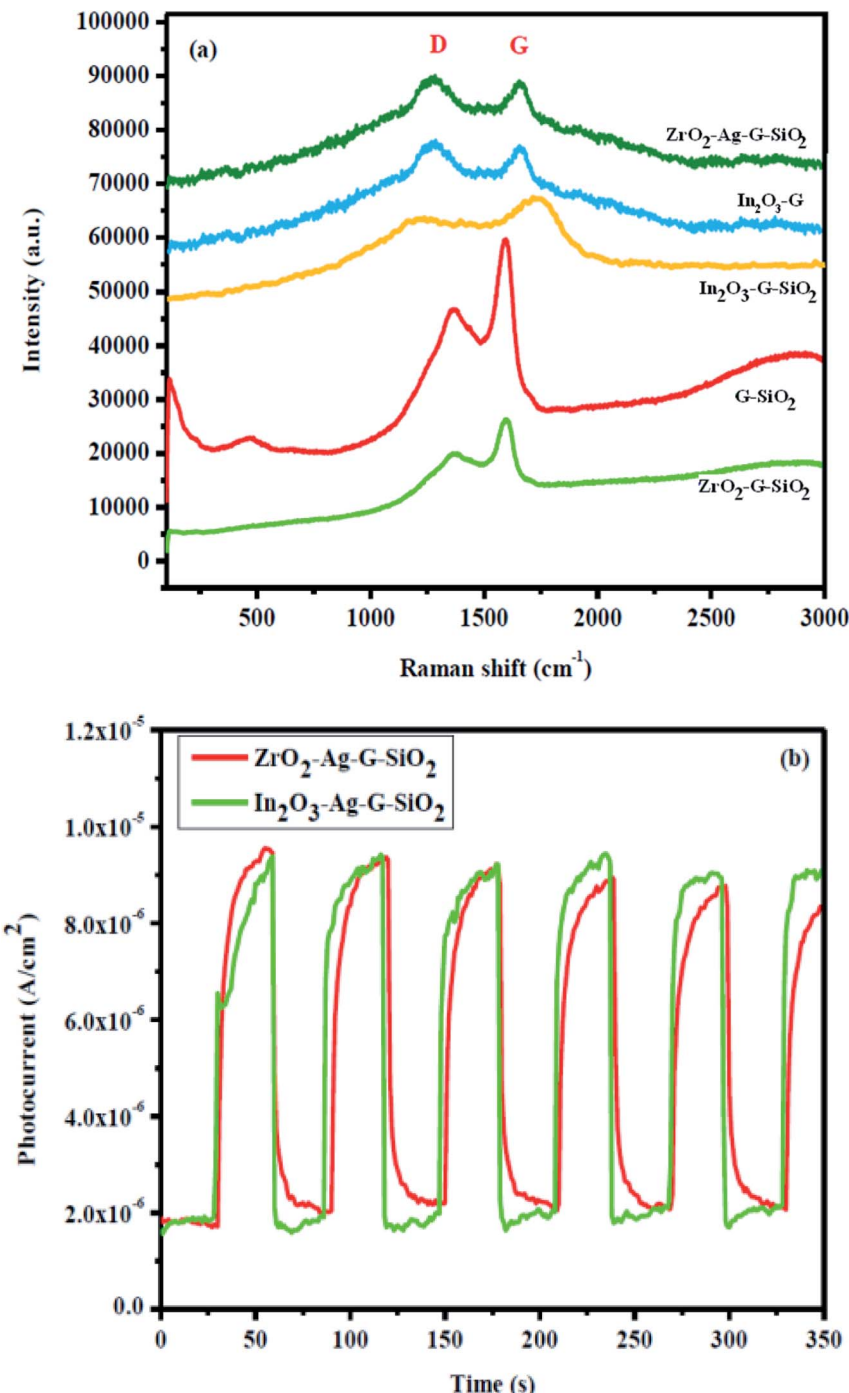


Fig. 5 Raman spectra of (a)  $\text{In}_2\text{O}_3$ -GO, G-SiO<sub>2</sub>, Zr-G-SiO<sub>2</sub>,  $\text{In}_2\text{O}_3$ -GO-SiO<sub>2</sub>, Zr-Ag-G-SiO<sub>2</sub>. (b) Photocurrent density of  $\text{In}_2\text{O}_3$ -GO-SiO<sub>2</sub>, Zr-Ag-G-SiO<sub>2</sub>.

graphene, and it appeared as a light dark shaded region. For a high-magnification HRTEM, Fig. 4B(a2) shows  $\text{In}_2\text{O}_3$ -GO-SiO<sub>2</sub> nanoparticles, and glass-like cross-section borders with the  $d$ -dispersing of 0.29 Å compared to  $\text{In}_2\text{O}_3$  (222); (b2) shows Zr-Ag-G-SiO<sub>2</sub> translucent grid borders with the  $d$ -separating of 0.462 Å nm, relating to (202). Further details of the translucent grid were observed in selected area electron diffraction (SAED) examination, as shown in Fig. 4B(b1) and (b2). The patterns uncover three concentric diffraction rings from the centre

corresponding to  $\text{In}_2\text{O}_3$ -GO-SiO<sub>2</sub> (211), (222), and (400), and Zr-Ag-G-SiO<sub>2</sub>, (112), (103) and (202), respectively. The calculation of interplanar spacing depends on the structural phase of the material. If the interplanar spacing ( $d$  spacing) is reduced, the planes ( $hkl$ ) are expanded.

Raman spectroscopy is a light scattering technique, where the laser light interacts with sub-atomic vibrations and photons bringing about a change in the energy, either increase or decrease, of the laser photons. The results of Raman



spectroscopy provide data on the electronic band structure of (D and G band) carbon materials, phases and fundamental properties of the spherical phase of  $\text{SiO}_2$ , cubic phase of  $\text{ZrO}_2$ , and

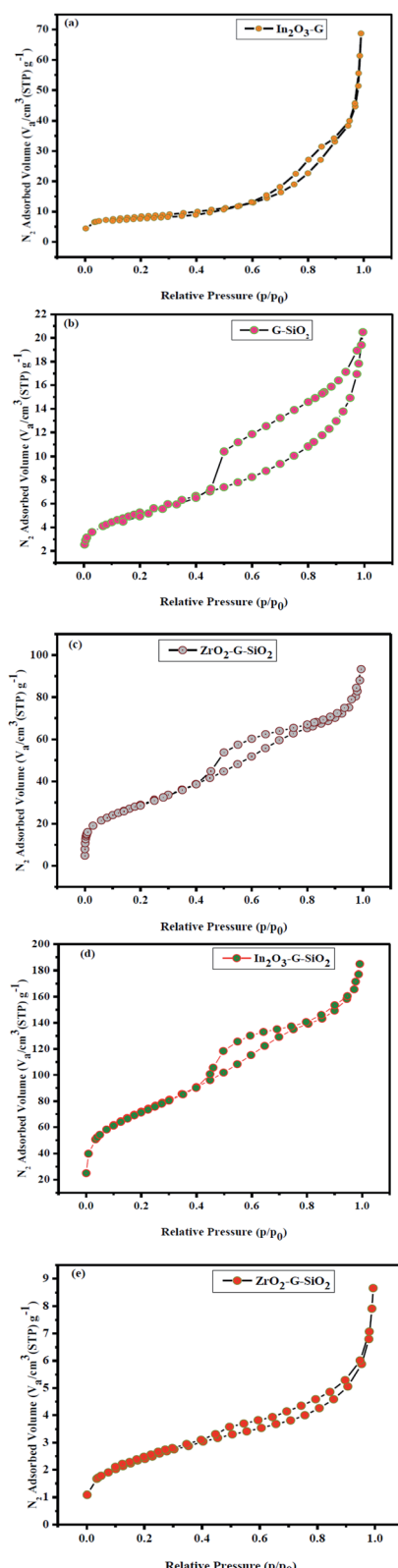


Fig. 6 Nitrogen adsorption–desorption isotherms of (a)  $\text{In}_2\text{O}_3$ –GO, (b) G– $\text{SiO}_2$ , (c) Zr–G– $\text{SiO}_2$ , (d)  $\text{In}_2\text{O}_3$ –GO– $\text{SiO}_2$ , (e) Zr–Ag–G– $\text{SiO}_2$ .

graphene because of the solid scattering properties, as shown in Fig. 5. Zirconium oxide ( $\text{ZrO}_2$ ) has three different crystalline phases, (a) monoclinic 18 ( $9\text{A}_g + 9\text{B}_g$ ), (b) tetragonal 6 ( $1\text{A}_{1g} + 2\text{B}_{1g} + 3\text{E}_g$ ), and (c) cubic 3 ( $\text{T}_{2g}$ ) vibrational modes.<sup>20</sup> The  $\text{ZrO}_2$  peak (green colored) was located in the wavelength range of  $100$ – $800$   $\text{cm}^{-1}$ . The vibrational modes of the monoclinic phase were allocated as follows:  $\text{A}_g$  at  $177$ ,  $333$ ,  $346$ ,  $476$   $\text{cm}^{-1}$ ,  $\text{B}_g$  at  $501$ ,  $637$ ,  $756$   $\text{cm}^{-1}$ , and the shifts at  $476$  and  $637$   $\text{cm}^{-1}$  belong to the biphasic structure.<sup>21</sup> The GO– $\text{SiO}_2$  binary composite exhibited 3 unique peaks (orange colored), which appeared at wavelengths of  $510$ ,  $1363$ , and  $1590$   $\text{cm}^{-1}$ . The wide and low-intensity peak was situated at a wavelength of  $510$   $\text{cm}^{-1}$ , which corresponds to the spherical structure of  $\text{SiO}_2$ , while the other two peaks were allocated to the D and G-band of graphene. As a rule, the D-band was at the wavelength of  $1390$   $\text{cm}^{-1}$  and the G-band was at around  $1583$   $\text{cm}^{-1}$  because of the  $\text{E}_{2g}$  mode of graphene.<sup>22</sup> The peak properties of the D and G bands (position, intensity, and width) are used for characterizing material composition. In the Raman spectrum of GO– $\text{SiO}_2$ , the main peak appeared at  $1363$   $\text{cm}^{-1}$  and the peak can be attributed to the ordinary  $\text{sp}^3$  hybridized carbon (D band) auxiliary defect, while the subsequent peak can be attributed to the in-plane vibration of  $\text{sp}^2$  hybridized carbons (G band) that was located at  $1590$   $\text{cm}^{-1}$  (graphite), and can be used to characterize the arrangement of the electronic structure of graphene. The Raman spectrum of  $\text{ZrO}_2$ –GO– $\text{SiO}_2$  with the characteristic peaks of graphene were observed, while the peaks of  $\text{SiO}_2$  and  $\text{ZrO}_2$  were not present. Peaks appeared at  $1370$   $\text{cm}^{-1}$  and  $1597$   $\text{cm}^{-1}$  Raman wavelengths, and the peak intensity was lower than the intensity of the D and G-groups. In the consequent Raman spectrum, the position of the D and G-band was changed, which was expected of the  $\text{SiO}_2$  and  $\text{ZrO}_2$  attached to the surface of graphene, implying that the composition of graphene was changed. The intensity of the D-band was lower than that of the G-band, implying that there were more  $\text{sp}^2$  bonds and more change from  $\text{sp}^3$  to  $\text{sp}^2$ . Besides, the intensity ratio of  $I_{\text{D}}/I_{\text{G}}$  determined the  $\text{sp}^3/\text{sp}^2$  proportion of graphene, and the value was 1.04. Fig. 5(b) shows the photo-current response of the ternary composite during four on-off cycles of light illumination. Generally, the ternary composite showed rapid and high-velocity current response for each light irradiation.<sup>23</sup> This shows the improvement of the high sensing activity of the ternary composite.

The  $\text{N}_2$  adsorption–desorption isotherms were examined at  $77$  K for the as-obtained binary and ternary composites, as shown in Fig. 6. The surface area and pore-size distribution were assessed by BET and BJH methods, respectively. The

Table 1 Surface properties of the obtained  $\text{In}_2\text{O}_3$ –GO,  $\text{In}_2\text{O}_3$ –GO– $\text{SiO}_2$ , G– $\text{SiO}_2$ , Zr–G– $\text{SiO}_2$  and Zr–Ag–G– $\text{SiO}_2$

Samples	BET surface area ( $\text{m}^2 \text{g}^{-1}$ )	Total pore volume ( $\text{cm}^3 \text{g}^{-1}$ )	Average Pore diameter (nm)
$\text{In}_2\text{O}_3$ –GO	29.688	0.105	13.995
$\text{In}_2\text{O}_3$ –GO– $\text{SiO}_2$	253.79	0.281	4.4284
G– $\text{SiO}_2$	33.250	0.145	14.213
Zr–G– $\text{SiO}_2$	106.205	0.123	5.6691
Zr–Ag–G– $\text{SiO}_2$	9.1703	0.020549	8.9632



results are shown in Fig. 6, while the summarized information is presented in Table 1. The overall weight of the hysteresis loops was  $(0.4\text{--}1.0) P/P_0$ , as shown in Fig. 6(a). The adsorption isotherm of  $\text{ZrO}_2\text{-GO}$  binary composite corresponds to type II

isotherm (nonporous or macroporous), while the relationship between the pore shape and the adsorption–desorption isotherm indicate H3 hysteresis. The type H3 hysteresis loop indicates or corresponds to a slit-like pore. The  $\text{GO-SiO}_2$  binary

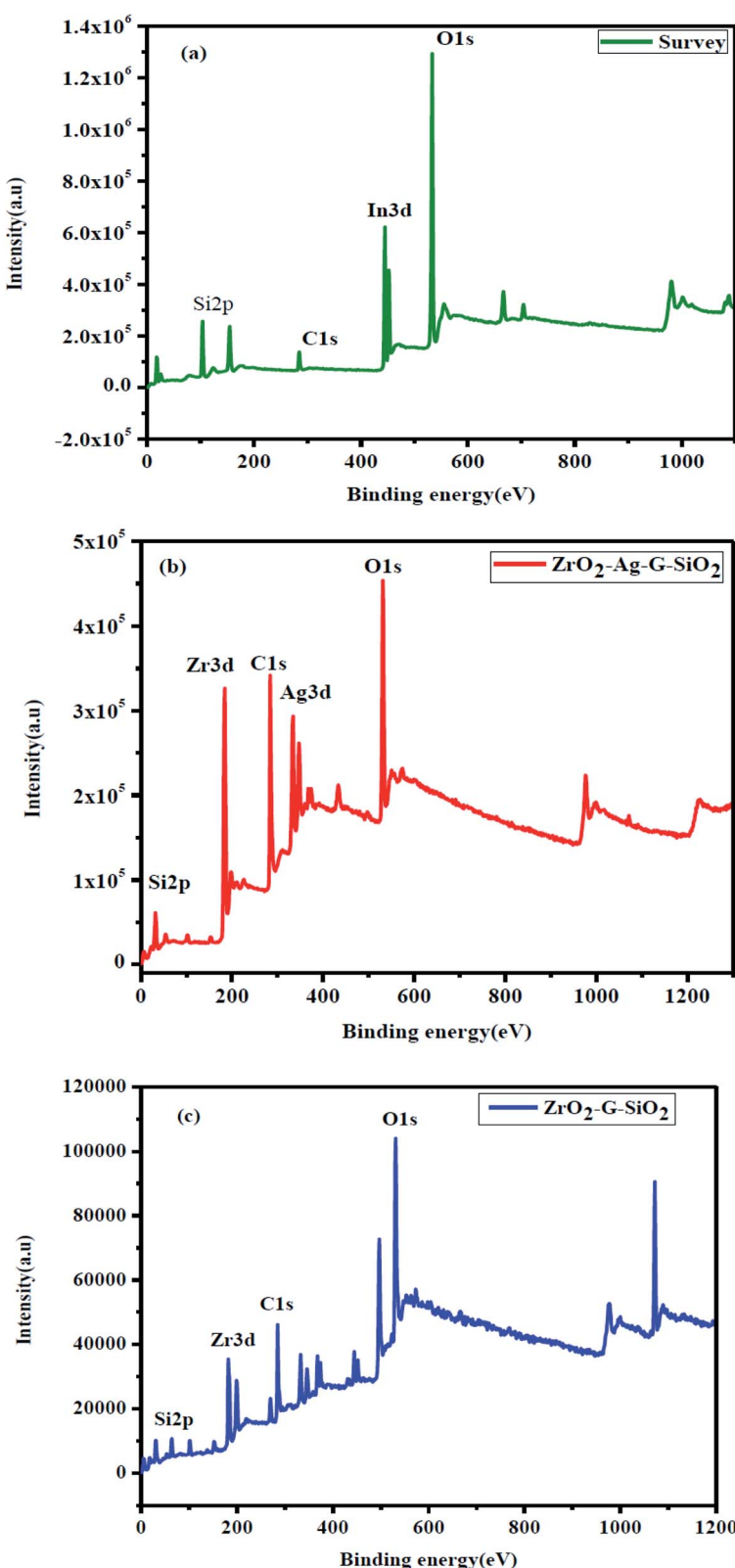


Fig. 7 XPS spectra of (a)  $\text{In}_2\text{O}_3\text{-GO-SiO}_2$ , (b)  $\text{Zr-Ag-G-SiO}_2$ , (c)  $\text{Zr-G-SiO}_2$ .

composite was identified with type IV isotherm with type H1 hysteresis loop. The adsorption isotherm of  $\text{ZrO}_2$ -GO-SiO<sub>2</sub> ternary composite exhibited type IV isotherm with type H1 hysteresis loop. The type IV isotherm is normal for mesoporous adsorbents.<sup>27</sup> The ternary  $\text{ZrO}_2$ -GO-SiO<sub>2</sub> composite has a greater surface area,  $106.205 \text{ m}^2 \text{ g}^{-1}$ , while the normal pore breadth was 5.4 nm. The spherical SiO<sub>2</sub> attached to  $\text{ZrO}_2$ -GO because of the improved value of the specific surface area and the experimental conditions, particularly the calcination temperature. The obtained ternary composite had a high specific surface area and approximately small pores, which exhibit high synergy between the environment of the composite and color material during the degradation cycle. The excellent performance of these mesoporous materials was attributed to a high surface area, tunable pore size, and increased number of active sites of the nano-sized substrate material. High surface area and mesoporosity are directly related to the high adsorption capacity of sensing materials. The hysteresis loops gradually shift to a higher relative pressure ( $P/P_0$ ) for  $\text{In}_2\text{O}_3$ -GO-SiO<sub>2</sub> and  $\text{ZrO}_2$ -GO-SiO<sub>2</sub> suggesting that these mesopores were expanding the mesoporous SiO<sub>2</sub>.

Fig. 7(a) shows the XPS spectra which confirmed the interaction between  $\text{ZrO}_2$ , SiO<sub>2</sub>, and graphene. XPS investigation was performed over ternary  $\text{ZrO}_2$ -GO-SiO<sub>2</sub> composite. Fig. 7(b) shows the XPS spectrum of O 1s, where the peak is at a binding energy of around 531 eV; the peak can be attributed to metal oxide ions; on the other hand, if the binding energy of the peak is higher than 531 eV, it corresponds to hydroxide ions.<sup>23</sup> In the XPS spectrum of O 1s, the wide peak was located at 530.79 eV, and the binding energy was lower than 531 eV, demonstrating the type of metal oxide. Fig. 7(c) presents the XPS spectrum of C 1s showing three peaks that were located at the binding energy values of 284.63, 285.65 and 288.38 eV. The XPS spectrum of C 1s comprises few characteristic peaks, such as carbonyl carbon (C=O, (288.4–288.6) eV), aliphatic (C-C, (284.4–285.9) eV), Zr–O–C ((286.6–286.8) eV), and carboxylate carbon (O–C=O, 289.3 eV).<sup>24</sup> The (C–C) and (C–C) bonds indicate the carbon-to-carbon chemical bonding state, and C–OX (X = metal) bond indicates the metal-to-carbon chemical bonding state. Fig. 7(d) shows the XPS spectrum of Zr 3d comprising two sharp peaks. These two peaks were located at binding energy values of 181.98 and 184.34 eV, attributed to the spin orbital type of Zr 3d<sub>5/2</sub> and Zr 3d<sub>3/2</sub>, and this result is the proof of Zr(4 – x) particles.<sup>25</sup> The XPS peaks of Si2p appeared at 101.60 eV binding energy region in Fig. 7(e) and this peak assigned to the presence of O–Si–O. The spins-orbital were not included in the XPS analysis due to peak distortion.<sup>26</sup> The binding energy shifts show the strong bonding between in  $\text{ZrO}_2$ -GO-SiO<sub>2</sub>.

### 3.2. Electrochemical response of $\text{ZrO}_2$ -Ag-G-SiO<sub>2</sub> and $\text{In}_2\text{O}_3$ -G-SiO<sub>2</sub>

Fig. 8(a) demonstrates the electrochemical properties of  $\text{ZrO}_2$ -Ag-G-SiO<sub>2</sub> and  $\text{In}_2\text{O}_3$ -G-SiO<sub>2</sub>, the CV curves of different electrodes with uncovered  $\text{In}_2\text{O}_3$ -G, G-SiO<sub>2</sub>,  $\text{ZrO}_2$ -G-SiO<sub>2</sub>,  $\text{ZrO}_2$ -Ag-G-SiO<sub>2</sub> and  $\text{In}_2\text{O}_3$ -G-SiO<sub>2</sub> electrode in 0.2 M PBS (pH  $\frac{1}{4}$  7.0). Fig. 8(b) shows that, in contrast with the absence of glucose, the increase in the oxidation current due to the increase in glucose

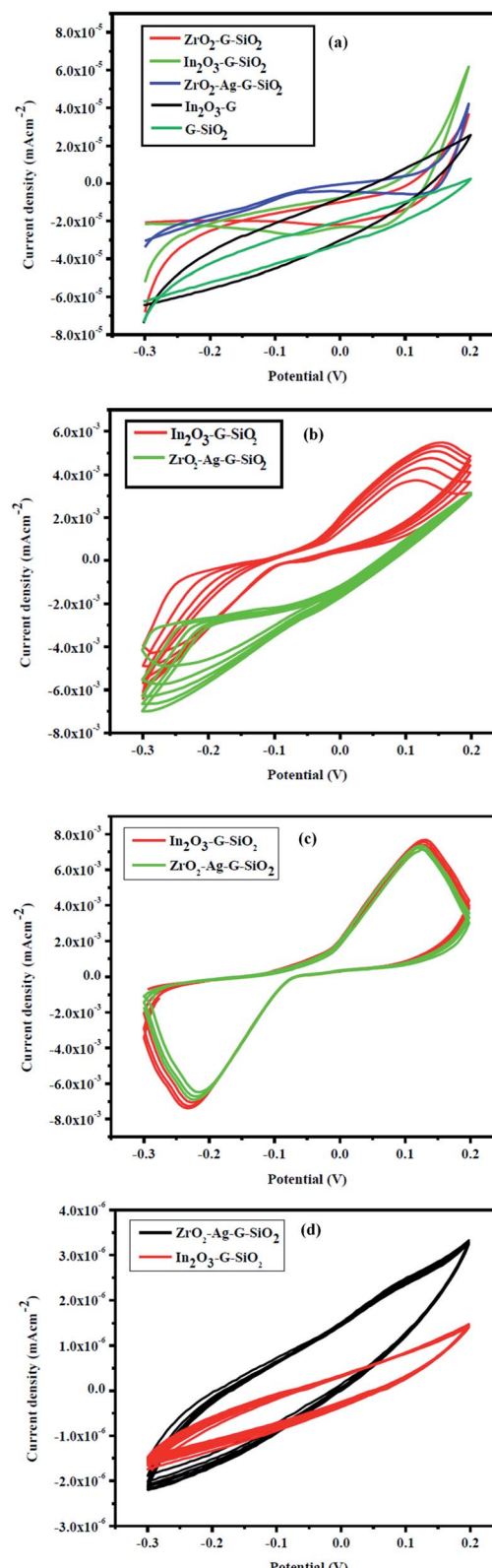


Fig. 8 (a) Cyclic voltammograms of  $\text{In}_2\text{O}_3$ -GO, G-SiO<sub>2</sub>,  $\text{Zr}$ -G-SiO<sub>2</sub>,  $\text{In}_2\text{O}_3$ -GO-SiO<sub>2</sub>,  $\text{Zr}$ -Ag-G-SiO<sub>2</sub> in PBS. (b)  $\text{In}_2\text{O}_3$ -GO-SiO<sub>2</sub>,  $\text{Zr}$ -Ag-G-SiO<sub>2</sub> with glucose, (c) with ascorbic acid and (d) with albumin.



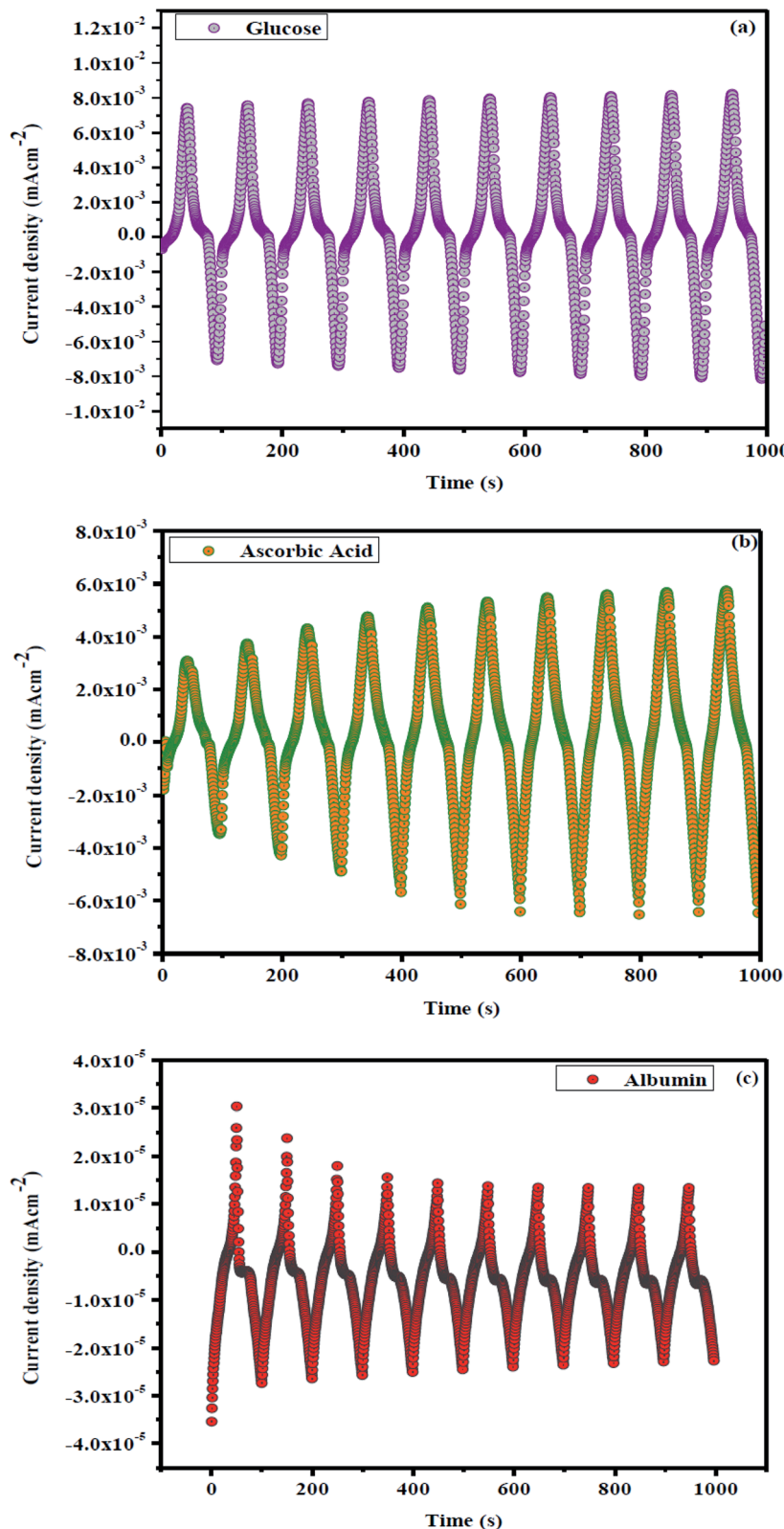


Fig. 9 (a) Concentration dependency of  $\text{In}_2\text{O}_3$ -GO with glucose, (b) with ascorbic acid (c) albumin.

concentration occurred on account of  $\text{ZrO}_2$ -Ag-G-SiO<sub>2</sub> and  $\text{In}_2\text{O}_3$ -G-SiO<sub>2</sub>. Fig. 8(c) shows the oxidation current of AA,  $\text{ZrO}_2$ -Ag-G-SiO<sub>2</sub> and  $\text{In}_2\text{O}_3$ -G-SiO<sub>2</sub> display a verified increment at 0.1 V while the other three anodes showed a slight change in the

studied low potential range containing 1.0 mM AA. The enhanced electrocatalytic performance of  $\text{In}_2\text{O}_3$ -G-SiO<sub>2</sub> might be due to its synergistic effect and higher electrochemically active surface area compared to other anodes. The mesoporous



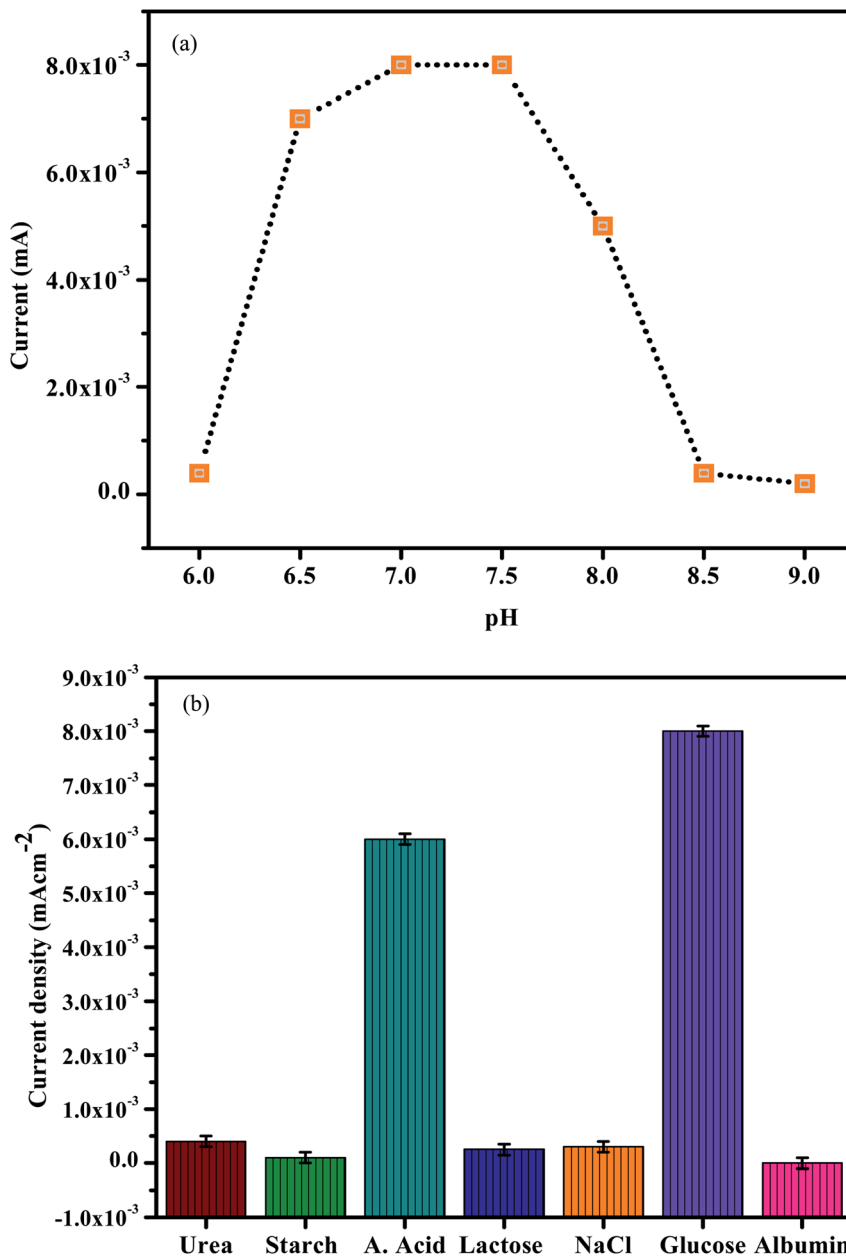


Fig. 10 (a) The electrochemical response of the presented sensor in 0.2 M PBS at different pH. (b) Selectivity of the sensor.

structure of spherical  $\text{In}_2\text{O}_3$ –G– $\text{SiO}_2$  can provide a large active area for the oxidation state of glucose and AA and the structure can improve the mass exchange. In Fig. 8(d), the oxidation current at  $\text{ZrO}_2$ –Ag–G– $\text{SiO}_2$  and  $\text{In}_2\text{O}_3$ –G– $\text{SiO}_2$  show a significant decline at 0.1 V in the presence of albumin.

For more information on synergistic activity, clinically negative control urine was used to assess non-enzymatic electrochemical sensitivity to glucose. Fig. 9 shows the concentration dependency of  $\text{In}_2\text{O}_3$ –GO with glucose, ascorbic acid and albumin. Fig. 9 shows an oxidation current decreasing from 0 to 0.8 V, which indicates that the oxidation current expands slightly in  $\text{In}_2\text{O}_3$ –G– $\text{SiO}_2$ , which strengthens the egg white and has less reactivity. Fig. 10(a) and (b) show pH dependency of  $\text{In}_2\text{O}_3$ –G– $\text{SiO}_2$  in PBS. In Fig. 10(a) and (b), both curves of  $\text{In}_2\text{O}_3$ –

G– $\text{SiO}_2$  show expanding oxidation current patterns with respect to increasing glucose concentration from 0 to 3 mM in PBS.

### 3.3. Catalytic performance and detection mechanism in physiological pH

To enhance the electrochemical reaction of  $\text{In}_2\text{O}_3$ –G– $\text{SiO}_2$  for glucose, AA and microalbumin detection, the effect of pH on the electrode reaction was studied by CV in 0.2 M PBS containing 1.0 mM Glucose, AA and microalbumin at various pH. A significant increase in the current signal was observed with the increase in pH and showed the best performance at pH 7.0 (Fig. 10(a)). The result likewise shows that AA can be detected at different pH. This might be credited to the excellent stability of

the incorporated  $\text{In}_2\text{O}_3\text{-G-SiO}_2$ , which may enhance the capacity to oppose the external condition. Furthermore, since the electrode materials are altogether inorganic materials, in contrast to the organic catalysts, they are less affected by the external condition. To maintain the physiological condition and acquire high sensitivity, pH 7.0 PBS was chosen for further experiments.

### 3.4 Interference

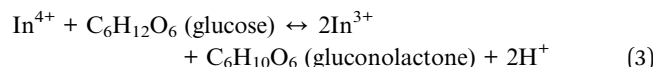
To assess the selectivity of  $\text{In}_2\text{O}_3\text{-G-SiO}_2$ , we studied the effect of various interfering ions and organic molecules in the electrochemical trials (Fig. 9(b)). No interference was observed for starch, KCl, albumin, UA, urea, glucose, and NaCl when their concentrations were multiple times higher than that of AA (0.2 mM). The high selectivity could be due to the superimposed active sites of the incorporated electrode having a strong synergistic effect on the oxidative dehydrogenation of ascorbic acid and glucose, and furthermore, mostly in light of the fact that  $\text{In}_2\text{O}_3\text{-G-SiO}_2$  coordinated electrode has no obvious reactant effect on the expected interfering substances in dietary items or other organic samples. The results show the interference capacity of  $\text{In}_2\text{O}_3\text{-G-SiO}_2$ .

### 3.5 Reproducibility and stability of the developed sensor

The reproducibility of the sensor was also explored for three estimations with increasing glucose, AA, and albumin concentration. The relative standard deviation (RSD) of the current signal for 1.0 mM AA was under 2%. When  $\text{In}_2\text{O}_3\text{-G-SiO}_2$  was stored at room temperature for 30 days, it showed that the current reaction to 1.0 mM AA retained 98.2% of its initial capacity, demonstrating excellent electrochemical stability of the electrode. As shown in Table 1,  $\text{In}_2\text{O}_3\text{-G-SiO}_2$ -nanocomposites had a high surface area and pore size, and their sensing activity to glucose and AA was high due to these properties. In addition, the stability and reproducibility of the sensor were high, and it indicates that the field of application of this material is wide.

### 3.6 Catalytic performance and detection mechanism

According to Fig. 7–10, there were 3 oxidation potentials located at 0.18, 0.42, and 0.88 V corresponding to non-enzymatic glucose and ascorbic acid detection in urine. The feasible component of  $\text{In}_2\text{O}_3\text{-G-SiO}_2$  depended on the electrooxidation of pre-monolayer hydroxyl Co active sites and oxide arrangement of  $\text{In}_2\text{O}_3$ . The synergistic significance of the OH-ads layer was observed to mediate oxidation, followed by chemisorption of glucose.<sup>30</sup> These peaks were attributed to the reduction/oxidation of  $\text{In}^{2+}/\text{In}^{3+}$  and redox couples. Then, the glucose oxidation kinetics of  $\text{InOOH}$  was studied along with the charge/discharge profiles of other important species, indicating the decrease of oxygen release in glucose alternatives at a high potential above 0.8 V.<sup>8</sup> In neutral pH urine,  $\text{In}_2\text{O}_3$  could poorly bond to the hydroxyl ions. Our results demonstrated the presence of  $\text{In}^{2+}/\text{In}^{3+}$  redox couples. Hence, our proposed detection system of  $\text{In}_2\text{O}_3\text{-G-SiO}_2$  is summarized in eqn (2) and (3).



## 4. Conclusions

In this study, we prepared mesoporous  $\text{ZrO}_2\text{-GO-SiO}_2$  and  $\text{In}_2\text{O}_3\text{-G-SiO}_2$  materials and evaluated their performance for glucose, ascorbic acid, and albumin detection in the concentration range from 0 to 3 mM. With the necessity of a strong alkaline condition,  $\text{In}_2\text{O}_3\text{-G-SiO}_2$  with high surface area and adsorption capacity demonstrated a comparable performance for electrochemical reactions using cyclic voltammetry. The both direct synergistic oxidation of the  $\text{In}^{3+}/\text{Co}^{4+}$  oxidation-oxide pair and manual oxidation were studied by measuring glucose. In view of the results,  $\text{In}_2\text{O}_3\text{-G-SiO}_2$  exhibited excellent sensitivity in urine, recommending practical application for glucose estimation in urine.

## Conflicts of interest

There are no conflict to declare.

## Acknowledgements

This work was supported by the Research Foundation of Hanseo University in 2020. The authors are grateful to the staff of the University for financial support.

## References

- W. Animaw and Y. Seyoum, Increasing prevalence of diabetes mellitus in a developing country and its related factors, *PLoS One*, 2017, **12**, e0187670.
- C. Radhakumary and K. Sreenivasan, Naked eye detection of glucose in urine using glucose oxidase immobilized gold nanoparticles, *Anal. Chem.*, 2011, **83**, 2829–2833.
- M. S. Kim and D.-Y. Lee, Urinary glucose screening for early detection of asymptomatic type 2 diabetes in Jeonbuk Province Korean schoolchildren, *J. Korean Med. Sci.*, 2017, **32**, 985–991.
- N. Friedrich, T. Skaaby, M. Pietzner, K. Budde, B. H. Thuesen, M. Nauck and A. Linneberg, Identification of urine metabolites associated with 5-year changes in biomarkers of glucose homoeostasis, *Diabetes Metab.*, 2018, **44**, 261–268.
- P. Si, Y. Huang, T. Wang and J. Ma, Nanomaterials for electrochemical non-enzymatic glucose biosensors, *RSC Adv.*, 2013, **3**, 3487–3502.
- K. Tian, M. Prestgard and A. Tiwari, A review of recent advances in nonenzymatic glucose sensors, *Mater. Sci. Eng., C*, 2014, **41**, 100–118.
- D. Pletcher, Electrocatalysis: present and future, *J. Appl. Electrochem.*, 1984, **14**, 403–415.



8 K. E. Toghil and R. G. Compton, Electrochemical non-enzymatic glucose sensors: a perspective and an evaluation, *Int. J. Electrochem. Sci.*, 2010, **2010**, 1246–1301.

9 S. Fu, G. Fan, L. Yang and F. Li, Non-enzymatic glucose sensor based on Au nanoparticles decorated ternary Ni–Al layered double hydroxide/single-walled carbon nanotubes/graphene nanocomposite, *Electrochim. Acta*, 2015, **152**, 146–154.

10 L. T. Hoa, K. G. Sun and S. H. Hur, highly sensitive non-enzymatic glucose sensor based on Pt nanoparticle decorated graphene oxide hydrogel, *Sens. Actuators, B*, 2015, **210**, 618–623.

11 G.-h. Wu, X.-h. Song, Y.-F. Wu, X.-m. Chen, F. Luo and X. Chen, Non-enzymatic electrochemical glucose sensor based on platinum nanoflowers supported on graphene oxide, *Talanta*, 2013, **105**, 379–385.

12 L. Hou, H. Zhao, S. Bi, Y. Xu and Y. Lu, Ultrasensitive and highly selective sandpaper-supported copper framework for non-enzymatic glucose sensor, *Electrochim. Acta*, 2017, **248**, 281–291.

13 X. Liu, W. Yang, L. Chen and J. Jia, Three-dimensional copper foam supported CuO nanowire arrays: an efficient non-enzymatic glucose sensor, *Electrochim. Acta*, 2017, **235**, 519–526.

14 Y. Zhong, T. Shi, Z. Liu, S. Cheng, Y. Huang, X. Tao, G. Liao and Z. Tang, Ultrasensitive non-enzymatic glucose sensors based on different copper oxide nanostructures by in situ growth, *Sens. Actuators, B*, 2016, **236**, 326–333.

15 Q. Wang, Q. Wang, M. Li, S. Szunerits and R. Boukherroub, Preparation of reduced graphene oxide/Cu nanoparticle composites through electrophoretic deposition: application for nonenzymatic glucose sensing, *RSC Adv.*, 2015, **5**, 15861–15869.

16 B. Hai and Y. Zou, Carbon cloth supported NiAl-layered double hydroxides for flexible application and highly sensitive electrochemical sensors, *Sens. Actuators, B*, 2015, **208**, 143–150.

17 X. Li, J. Liu, X. Ji, J. Jiang, R. Ding, Y. Hu, A. Hu and X. Huang, Ni/Al layered double hydroxide nanosheet film grown directly on Ti substrate and its application for a nonenzymatic glucose sensor, *Sens. Actuators, B*, 2010, **147**, 241–247.

18 Y. Shu, Y. Yan, J. Chen, Q. Xu, H. Pang and X. Hu, Ni and NiO nanoparticles decorated metal-organic framework nanosheets: facile synthesis and high-performance nonenzymatic glucose detection in human serum, *ACS Appl. Mater. Interfaces*, 2017, **9**, 22342–22349.

19 N. F. Zubair, S. Jamil, H. N. Bhatti and M. Shahid, A comprehensive thermodynamic and kinetic study of synthesized rGO–ZrO<sub>2</sub> composite as a photocatalyst and its use as fuel additive, *J. Mol. Struct.*, 2019, **1198**, 126869.

20 M. Rahsepar, F. Foroughi and H. Kim, A new enzyme-free biosensor based on nitrogen-doped graphene with high sensing performance for electrochemical detection of glucose at biological pH value, *Sens. Actuators, B*, 2019, **282**, 322–330.

21 N. Venkatathri, Synthesis of silica nanosphere from homogeneous and heterogeneous systems, *Bull. Mater. Sci.*, 2007, **30**, 615–617.

22 L. Wang, J. Zhao, H. Liu and J. Huang, Design modification and application of semiconductor photocatalysts, *J. Taiwan Inst. Chem. Eng.*, 2018, 590–602.

23 B. M. Mohammed, B. J. Fisher, D. Kraskauskas, S. Ward, J. S. Wayne, D. F. Brophy, A. A. Fowler, D. R. Yager and R. Natarajan, *Int. Wound J.*, 2015, 1–13.

24 M. Levavasseur, C. Becquart, E. Pape, M. Pigeyre, J. Rousseaux, D. Staumont-Sallé and E. Delaporte, *Eur. J. Clin. Nutr.*, 2015, **69**, 1076–1077.

25 S. Sasazuki, S. Sasaki, Y. Tsubono, S. Okubo, M. Hayashi and S. Tsugane, *Eur. J. Clin. Nutr.*, 2006, **60**, 9–17.

26 N. Attallah, Y. Osman-Malik, S. Frinak and A. Besarab, *Am. J. Kidney Dis.*, 2006, **47**, 644–654.

27 Y. Song, C. Gong, D. Su, Y. Shen, Y. Song and L. Wang, A novel ascorbic acid electrochemical sensor based on spherical MOF-5 arrayed on a three-dimensional porous carbon electrode, *Anal. Methods*, 2016, **8**(10), 2290–2296.

28 K. N. Fatema, S. Sagadevan, Y. Liu, K. Y. Cho, C. H. Jung and W. C. Oh, New design of mesoporous SiO<sub>2</sub> combined In<sub>2</sub>O<sub>3</sub>-graphene semiconductor nanocomposite for highly effective and selective gas detection, *J. Mater. Sci.*, 2020, **55**(27), 13085–13101.

29 K. N. Fatema, M. R. U. D. Biswas, S. H. Bang, K. Y. Cho and W. C. Oh, Electroanalytical characteristic of a novel biosensor designed with graphene–polymer-based quaternary and mesoporous nanomaterials, *Bull. Mater. Sci.*, 2020, **43**, 121.

30 M. Janyasupab, C. W. Liu, N. Chanlek, S. Chio-Srichan, C. Promptmas and W. Surareungchai, A comparative study of non-enzymatic glucose detection in artificial human urine and human urine specimens by using mesoporous bimetallic cobalt-iron supported N-doped graphene biosensor based on differential pulse voltammetry, *Sens. Actuators, B*, 2019, **286**, 550–563.

